



Paleoceanography and Paleoclimatology

Supporting Information for

Multi-elemental Statistical Features of Early Paleogene Sediments from the Mid-latitude Eastern Indian Ocean

Yusuke Kuwahara^{1,2}, Kazutaka Yasukawa^{3,1}, Erika Tanaka^{4,3}, Kentaro Nakamura^{3,1,2}, Minoru Ikehara⁴, and Yasuhiro Kato^{1,2}

¹Department of Systems Innovation, School of Engineering, The University of Tokyo, ²Ocean Resources Research Center for Next Generation, Chiba Institute of Technology, ³Frontier Research Center for Energy and Resources, School of Engineering, The University of Tokyo, ⁴Marine Core Research Institute, Kochi University

Contents of this file

Texts S1–S4
Figures S1–S12
Captions for Tables S1–S5

Additional Supporting Information (Files uploaded separately)

Tables S1–S5

Introduction

Supporting information consists of 4 texts, 12 figures, and 5 tables. Supporting Tables S1–S5 are Microsoft Excel files, uploaded separately.

Text S1. Fundamentals of Independent Component Analysis (ICA)

In this study, we used independent component analysis (ICA), a powerful tool for extracting hidden statistical features from multivariate datasets. By applying ICA, the observed multivariate dataset was transformed into a linear combination of base vectors (independent components: ICs) with minimal statistical dependencies between each other. In the geochemical context, each extracted IC vector indicates specific directions along which the chemical compositions of the samples shift independently, irrespective of the absolute elemental contents.

The theoretical model of ICA can be described as follows:

$$\mathbf{X} = \mathbf{S}\mathbf{A} \quad (1)$$

where \mathbf{X} represents the $n \times m$ matrix of observation data (n : number of samples, m : number of elements), \mathbf{S} indicates an $n \times r$ matrix of independent components (r : the number of dimensions, which is equivalent to the number of ICs), whose columns correspond to each IC. \mathbf{A} in Eq. (1) indicates an $r \times m$ mixing matrix that transforms base vectors (\mathbf{S}) into observed data (\mathbf{X}).

First, the observed data matrix \mathbf{X} is centered and scaled as a standardized matrix ($\bar{\mathbf{X}}$), where the mean and standard deviation are 0 and 1, respectively. Then, $\bar{\mathbf{X}}$ was uncorrelated using a principal component analysis (PCA) algorithm and transformed into a “whitened” matrix (\mathbf{Z}) by normalizing it by the data variance along each principal component (PC). Subsequently, PCs in the whitened space are rotated via multiplication with orthogonal matrices until the projection of \mathbf{Z} on each axis yields histograms with a maximum non-Gaussian distribution. In this study, the non-Gaussianity was evaluated using negentropy $J(y)$, which is described as:

$$J(y) = [\mathbb{E}\{G(y)\} - \mathbb{E}\{G(v)\}]^2 \quad (2)$$

where function $G(y)$ is an exponential function:

$$G(y) = -\exp\left(-\frac{y^2}{2}\right) \quad (3)$$

In Eq. (2), y is a random variable in the whitened space, and v indicates a Gaussian variable with mean = 0 and variance = 1. $\mathbb{E}\{\}$ in Eq. (2) means expectation. Based on the central limit theory, we assumed that each axis could be regarded as the statistically independent base vectors (i.e., ICs) when J (i.e., non-Gaussianity) is maximized (Hyvärinen et al., 2001). The detailed formulation of ICA for applying to marine sediments is described by Yasukawa et al. (2016).

Text S2 Determination of the Number of ICs

As described in the main text, we initially performed ICA with six ICs, based on principal component analyses (PCA) results and “Guttman–Kaiser criterion” to capture meaningful geochemical signatures. However, extracting too many ICs may introduce

“meaningless” signatures, such as noise from analytical errors, thus complicating interpretation. Therefore, validating the number of ICs for extraction is important. To evaluate the effects of random initial values given in the fastICA algorithm, we conducted 100 computational runs. With six extracted ICs, the IC vectors projected into the element space converged well and consistently exhibited distinct directions, although IC5 showed relatively larger variation compared to the others (Supporting Figure S2a).

Increasing the number of extracted ICs from six to seven slightly increased the proportion of the total sample variances accounted for by all ICs to 90.2%. Subsequently, one of the original six ICs, the biogenic apatite-dominated IC2 (Figure 4b), split into two ICs (IC4 and IC5 in Supporting Figure S3). However, when the number of ICs reached seven, certain IC vectors exhibited different directions from the fundamental ICs across the multiple trials of ICA ($n = 100$; Supporting Figure S2b; red arrows). This observation suggests that the extracted ICs do not show robust convergence and may pick up some weak noise-affected signals from the dataset. Therefore, we concluded that the most appropriate number of ICs for our study is six.

Text S3. Comparing to the CIEs from other sites

Previously, hyperthermals characterized by the negative excursions of bulk carbonate $\delta^{13}\text{C}$ records have been reported from the Pacific, Atlantic, and Indian Oceans (Supporting Figure S8a, b). Here, we compared the magnitudes of carbon isotope excursions (CIE) identified at Hole 762C with those of other sites (Supporting Figure S8c).

The CIE magnitude during the H2 event at Hole 762C ($\sim 0.6\text{‰}$; Supporting Figure S8c) is comparable to the bulk carbonate data from northeastern Atlantic ($\sim 0.4\text{‰}$: DSDP Site 550; Cramer et al., 2003), northwestern Atlantic ($\sim 0.5\text{‰}$: Blake Nose – ODP Site 1051; Cramer et al., 2003), equatorial Atlantic ($\sim 0.4\text{‰}$: Demerara Rise – ODP Site 1258; Westerhold et al., 2017), southern Atlantic ($\sim 0.6\text{‰}$: Walvis Ridge – ODP Sites 1262, 1263, 1265, and 1267; Stap et al., 2009; Westerhold et al., 2017), and the southern Indian Ocean ($\sim 0.5\text{‰}$: Kerguelen Plateau – ODP Hole 738C, Broken Ridge – ODP Site 752; Yasukawa et al., 2017). However, records from the central Pacific ($\sim 0.3\text{‰}$: DSDP Site 577; Cramer et al., 2003; Luciani et al., 2016), the southern Pacific ($\sim 0.2\text{‰}$: Campbell Plateau – IODP Site U1553, Mead Stream, Dee Stream; Nicolo et al., 2007; Niederbockstruck et al., 2024), and low latitude Indian Ocean ($\sim 0.2\text{‰}$: Ninetyeast Ridge – IODP Hole U1443A; Barnett et al., 2020) exhibit smaller CIEs compared with that of Hole 762C.

Regarding the I1 Events, the CIE at Hole 762C ($\sim 0.7\text{‰}$) is comparable to data from other regions. Similar CIE magnitudes have been reported in the Atlantic ($\sim 0.7\text{‰}$: DSDP 550, ODP Sites 1051, 1258, 1262, 1263; Cramer et al., 2003; Westerhold et al., 2017), Pacific ($0.5\text{--}0.6\text{‰}$: DSDP 577, IODP Site U1553, Mead Stream, Dee Stream; Cramer et al., 2003; Nicolo et al., 2007; Niederbockstruck et al., 2024), and southern Indian Oceans ($\sim 0.6\text{‰}$: ODP Sites 752 and 738; Yasukawa et al., 2017). In Hole 762C, the CIE magnitude during the J event ($\sim 0.5\text{‰}$) is similar to that of the Atlantic record ($\sim 0.5\text{‰}$: DSDP 550, ODP Sites 1258, 1262, 1263; Cramer et al., 2003; Westerhold et al., 2017) and the Pacific record ($\sim 0.4\text{‰}$: DSDP 577, IODP Site U1553; Luciani et al., 2016; Niederbockstruck et al., 2024).

The largest CIE ($\sim 0.9\text{‰}$) observed during the ETM3 horizon in Core 25X of Hole 762C sediments is comparable to those recorded in the Atlantic ($0.6\text{--}1.5\text{‰}$: DSDP 550, ODP Sites 1258, 1262, 1263; Cramer et al., 2003; Westerhold et al., 2017), Pacific ($0.7\text{--}1.0\text{‰}$: DSDP 577, ODP Site 1215, IODP Site U1553; Leon-Rodriguez & Dickens, 2010; Luciani et al., 2016; Niederbockstruck et al., 2024), and southern Indian Ocean records ($\sim 0.9\text{‰}$: Site 752; Yasukawa et al., 2017). The magnitude of the small CIE identified as the L event at Hole 762C ($\sim 0.4\text{‰}$) is also similar to that observed in the Atlantic ($0.4\text{--}0.6\text{‰}$: DSDP 550, ODP Site 1258; Cramer et al., 2003; Westerhold et al., 2017) and Indian Ocean records ($\sim 0.4\text{‰}$: Site 752; Yasukawa et al., 2017). Overall, the magnitude of CIEs during Eocene hyperthermals tends to be larger in the Atlantic, smaller in the Pacific, and intermediate in the Indian Ocean.

Text S4. Interpretation of ICs Extracted from Bulk Chemical Composition

IC3: Dilution between Biogenic CaCO_3 and Detrital Components

The IC3 shows positive CaCO_3 and Sr loadings and negative loadings of most other elements (Figure 4c). The IC3 score plotted against age is similar to that of CaCO_3 abundances (Supporting Figure S11). These features indicate that the positive side of IC3 represents the biogenic CaCO_3 component that constitutes the main component of the Hole 762C sediment. As Sr is an alkaline earth metal that can be easily incorporated into biogenic carbonates, Sr is known to coexist with Ca in carbonate sediments (e.g., Plank & Langmuir, 1998; Rudnick & Gao, 2014). Conversely, elements showing distinct negative loadings (e.g., Mg, Al, Ti, Rb, Zr, Nb, Cs, Hf, Th, and light rare earth elements [LREEs]), which are commonly contained in aluminosilicates, indicate the contribution of detrital components. Therefore, IC3 appears to indicate a mixing relationship between biogenic CaCO_3 and detrital components as one of the major structures in our dataset.

IC2: Biogenic Calcium Phosphate

The IC2 shows positive loadings of P, Y, and REE except for Ce (Figure 4b). This feature indicates that the IC2 extracts a biogenic calcium phosphate (BCP) component in the sediment. Biogenic calcium phosphate, a common component in marine sediments, is contained in bones, teeth, and scales of marine vertebrates. As BCP effectively adsorbs REE and Y from ambient seawater, REE and Y are highly concentrated in BCP in marine sediments (Kashiwabara et al., 2014; Takaya et al., 2018; Toyoda & Tokonami, 1990). Indeed, the Al-normalized P and Y abundances of Hole 762C show identical profiles and have a strong positive correlation ($r = 0.91$; Supporting Figure S11), suggesting that the excess P and Y (or REE) relative to detrital materials can be explained by BCP contribution. Therefore, the significant positive loadings of P and REE in IC2 may reflect the influence of BCP on the bulk sediment composition. Additionally, the small Ce loading and large loadings of Y and heavy rare earth elements (HREEs) on the positive side of IC2 loadings appear to be a similar pattern to the shale-normalized REE+Y composition of seawater (Alibo & Nozaki, 1999). Therefore, the BCP components in Hole

762C sediment are considered to contain REE and Y of seawater origin. Notably, in the profiles of IC scores against depositional age (Figure 6; Supporting Figure S11), IC2 does not show a mirror profile of the CaCO_3 and IC3. Therefore, the variation of IC2 scores does not simply reflect a simple dilution of BCP abundance by biogenic CaCO_3 . Instead, it is controlled by various environmental factors that influence the accumulation rate of BCP at Hole 762C.

IC4: Diagenetic Signature on Carbonate

The IC4 demonstrates positive loadings of Mn and CaCO_3 (Figure 4d). The abundance of Mn has been utilized as an indicator of diagenetic processes because its solubility is affected by the redox conditions in the sediment. In the oxic environment, Mn occurs as MnO_2 in sediments; under reducing conditions caused by the consumption of dissolved oxygen via organic matter decomposition, Mn dissolves in pore water as Mn^{2+} (e.g., Burdige & Gieskes, 1983; Calvert & Pederson, 1993). In carbonate sediments, dissolved Mn^{2+} can be incorporated into or precipitated as $(\text{Mn}, \text{Ca})\text{CO}_3$ on biogenic CaCO_3 (e.g., Barras et al., 2018; Boyle, 1983; Thomson et al., 1986, 1993; Pälike et al., 2014). Based on these behaviors of Mn in marine sediments and the positive correlation between Mn and CaCO_3 in the IC4, the positive loadings of IC4 can be interpreted as the incorporation of Mn by CaCO_3 through the diagenetic process at Hole 762C. Overall, we interpreted that IC4 represents the diagenetic signature involving redox changes in the Hole 762C sediments.

IC1, IC5, IC6: Redox-related Behaviors of Metal Elements

IC1, IC5, and IC6 are characterized by specific metals, including Co, Ni, U, Cu, Mo, Pb, Zn, and Sr (Figure 4a, e, f). The profiles of IC1, IC5, and IC6 scores exhibit spike-like excursions at horizons (e.g., hyperthermals), indicating that the concentration/depletion of these metal elements occurred at those horizons (Figure 7; Supporting Figure S12). These features suggest that IC1, IC5, and IC6 may indicate redox-related signatures in Hole 762C sediments because these metals exhibit specific abundances in sediments corresponding to the ambient redox state. The elements characterizing IC1, IC5, and IC6 (except Sr) are categorized as the “redox-sensitive elements” that exhibit characteristic reconcentration patterns in sediments due to the changes of valences corresponding to the redox state in the sediment pore water. Therefore, redox-sensitive elements are concentrated or depleted at the boundary between oxic and suboxic conditions in the sediments and utilized as the indicator of the redox state in the sediments (e.g., Calvert & Pederson, 1993; Thomson et al., 1993).

Various behaviors of such redox-sensitive metals have been proposed to explain their concentration/depletion in marine sediments, including remobilization and precipitation of metals due to the change of valence corresponding to the redox state of sediment pore water (e.g., Calvert & Pederson, 1993) and co-precipitation with authigenic pyrite (Algeo & Maynard, 2004; Huerta-Diez & Morse, 1992). The separation

between IC1, IC5, and IC6 may reflect differences in the concentration/depletion processes described above.

IC1 is characterized by positive Co, Ni, and U loadings, with its score indicating positive excursions at horizons near Hiatus D (55.857–54.739 Ma), I1 (53.665 Ma), and J (53.260 Ma) (Figure 7a, b). The variation in IC1 closely correlates with Co/Al and Ni/Al profiles, except at the I1 horizon (Supporting Figure S12b, c), strongly suggesting that IC1 reflects the variation of Co and Ni in the sediments. The presence of authigenic pyrite and the positive loading of U (Figure 4a), indicating a reduced porewater environment, suggests that the peaks in IC1 scores, reflecting elevated Co and Ni abundances, may be associated with the precipitation of sulfides (e.g., pyrite) (Huerta-Diez & Morse, 1992; Swanner et al., 2019). Due to slower uptake kinetics compared to other redox-sensitive elements (e.g., Cu, Mo, and Pb; Algeo & Maynard, 2004), the peaks in IC1, corresponding to Co and Ni peaks, are likely due to these kinetic differences (Figure 7).

IC5 exhibits positive loadings of Cu, Mo, and Pb (Figure 4e), with its score showing positive excursions at the horizons near Hiatus D, H2, and I1 (Figure 7). Additionally, a sharp positive spike of IC5 is observed at 54.48 Ma (Supporting Figure S12a). Conversely, IC6 is characterized by the positive loadings of Zn, Sr, and Pb (Figure 4f), and its scores show positive excursions at horizons near Hiatus D, I1, and ETM3. In addition, the IC6 score shows two excursions during 41.17–40.71 Ma (Supporting Figure S12a). Based on the element assemblages of IC5 and IC6 and the behavior of their scores, the IC5 and IC6 may reflect the remobilization and reconcentration of redox-sensitive elements due to the change of redox (or pH) conditions in the sediments.

The enrichment of Co, Ni, Cu, Mo, Zn, and Pb in marine sediments is also caused by the co-precipitation of authigenic pyrite under reductive conditions, although the uptake speed varies by element (e.g., Algeo & Maynard, 2004; Huerta-Diez & Morse, 1992). Indeed, at the horizons showing positive peaks of IC1, IC5, and IC6, we observed authigenic pyrite grains as suggested by the onboard visual core description of Hole 762C sediments (Haq et al., 1990). Therefore, the excursions of these three ICs could also reflect the occurrence of pyrite precipitation. Although pyrite precipitation or redox-related valence changes of metal elements are difficult to distinguish from the bulk chemical composition, the variation, and excursions of IC1, IC5, and IC6 scores can be interpreted as the redox (and/or pH) changes in the pore water.

Based on the above discussion, we interpreted that IC1, IC5, and IC6 reflect the post-depositional processes related to the changes in the sediments' redox (or pH) conditions. Therefore, we consider these three ICs as an indicator of the geochemical condition of pore water.

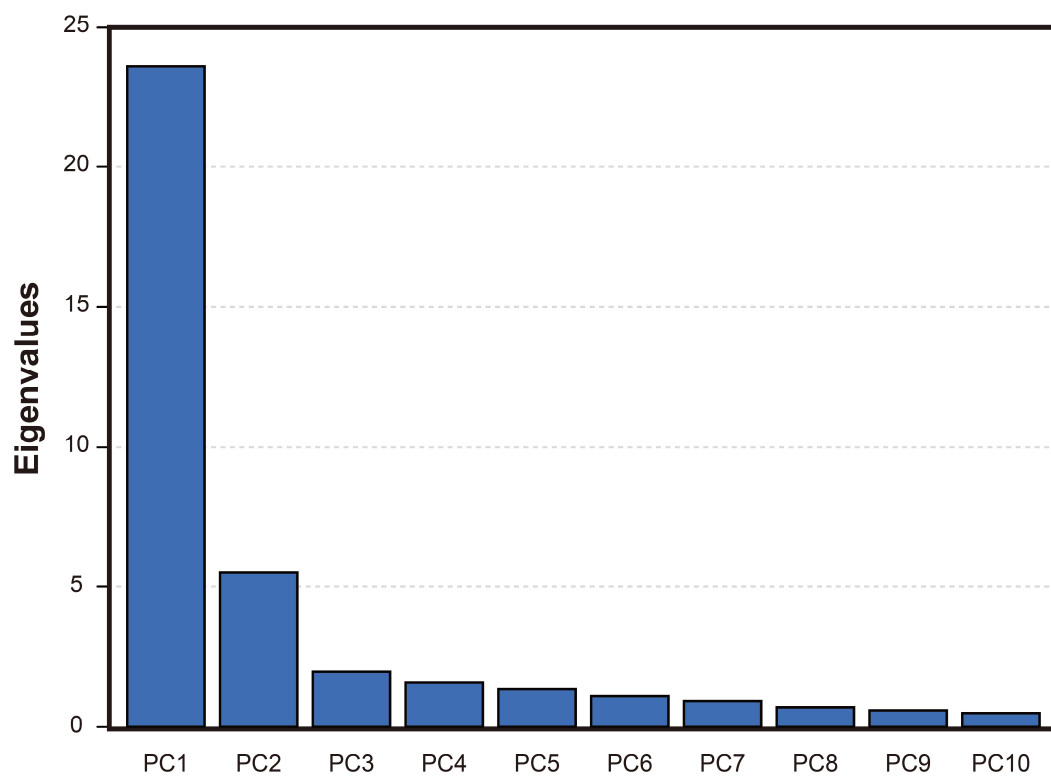


Figure S1. Eigenvalues of each principal component (PC) from Hole 762C dataset.

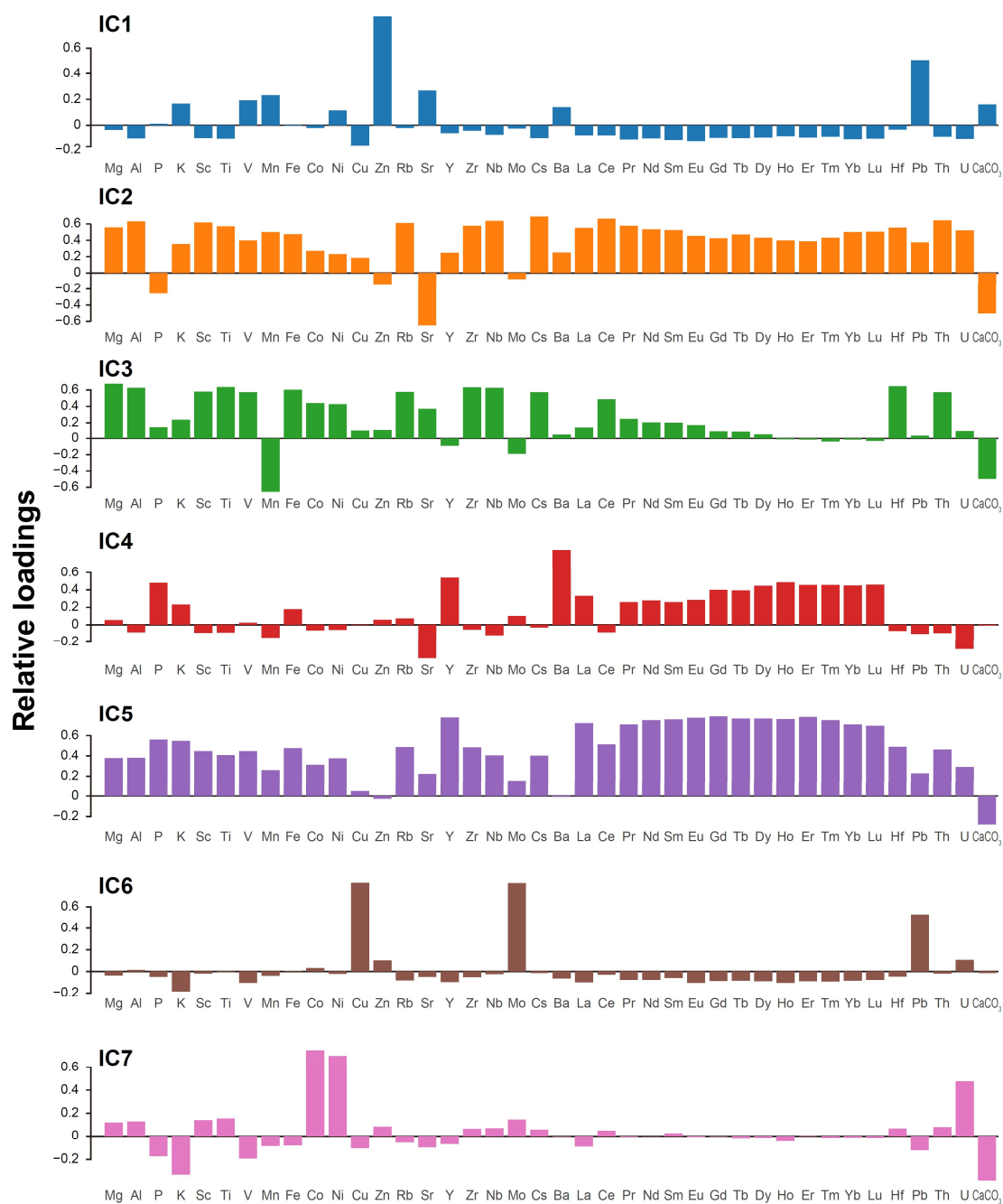


Figure S3. IC loadings of major and trace elements obtained from the Hole 762C datasets for seven ICs.

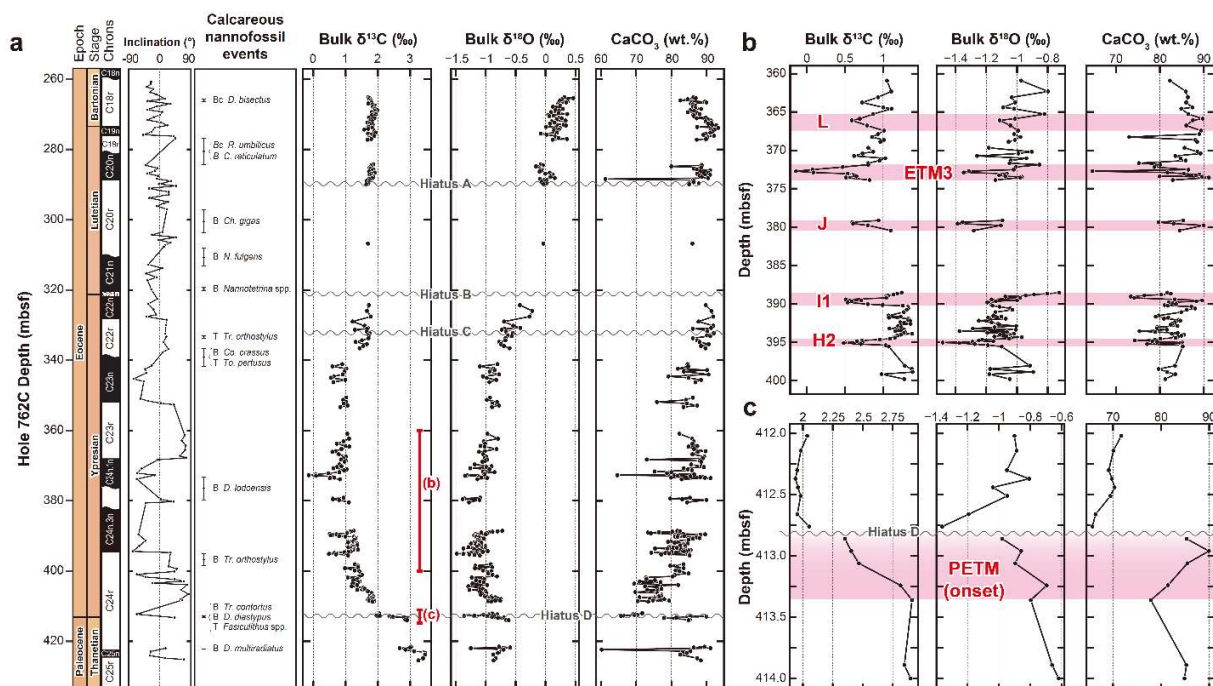


Figure S4. Depth profiles of bulk $\delta^{13}\text{C}$, $\delta^{18}\text{O}$, and CaCO_3 of Hole 762C. (a) All data. (b) Data from early Eocene (Core 25X–22X). (c) Data around Paleocene–Eocene boundary (Core 28X). Intervals with red lines indicate ranges of panels (b) and (c). Analytical uncertainties of $\delta^{13}\text{C}$ and $\delta^{18}\text{O}$ are less than 0.02‰ and 0.04‰, respectively. In panel (a), magneto-biostratigraphic columns are also shown (Galbrun, 1992; Shamrock and Watkins 2012).

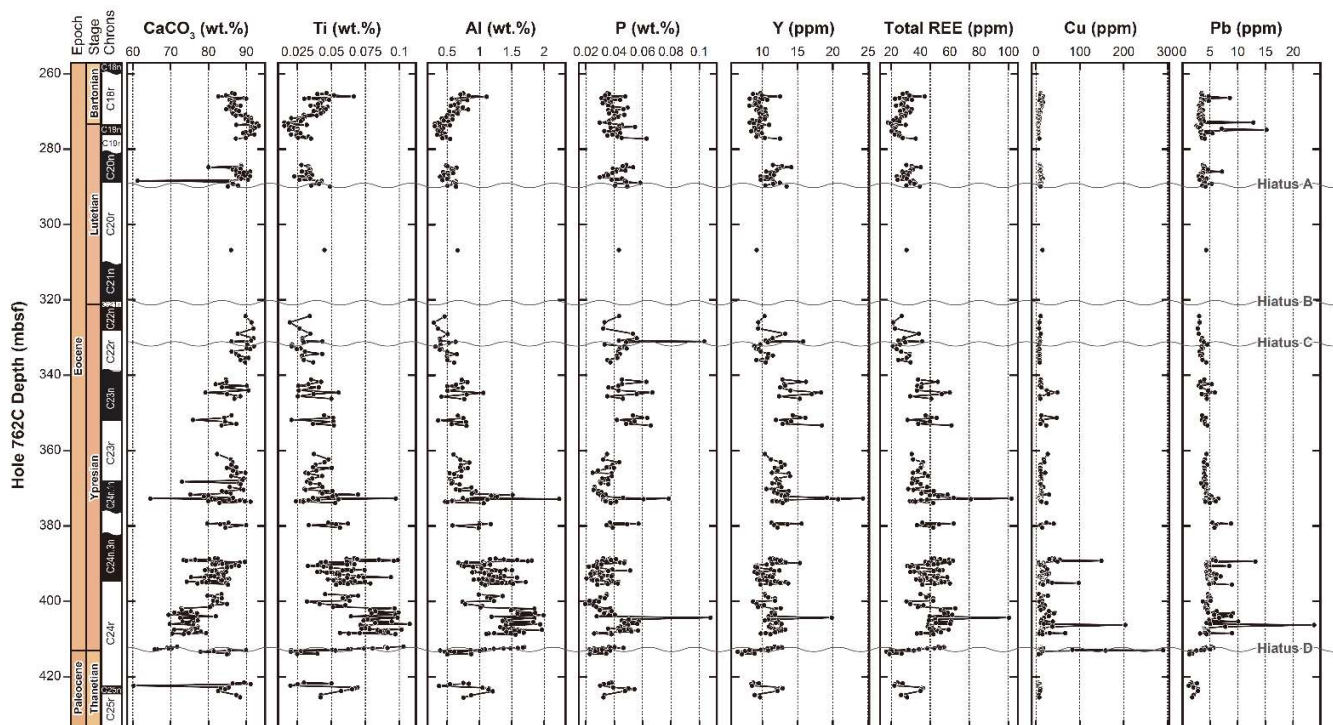


Figure S5. Depth profiles of CaCO_3 , Ti, Al, P, Y, total rare earth elements (REE), Cu, and Pb abundances of Hole 762C.

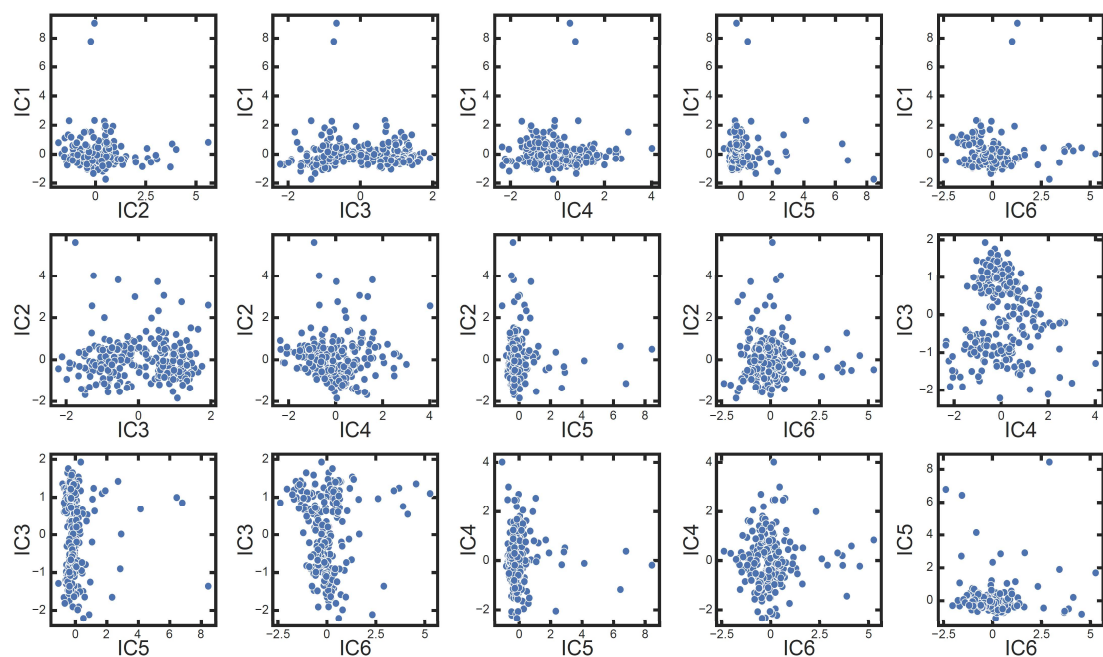


Figure S6. IC–IC pair plots of each IC of major- and trace-elements content obtained from Hole 762C datasets when the number of ICs = 6. The vertical and horizontal axes indicate IC scores.

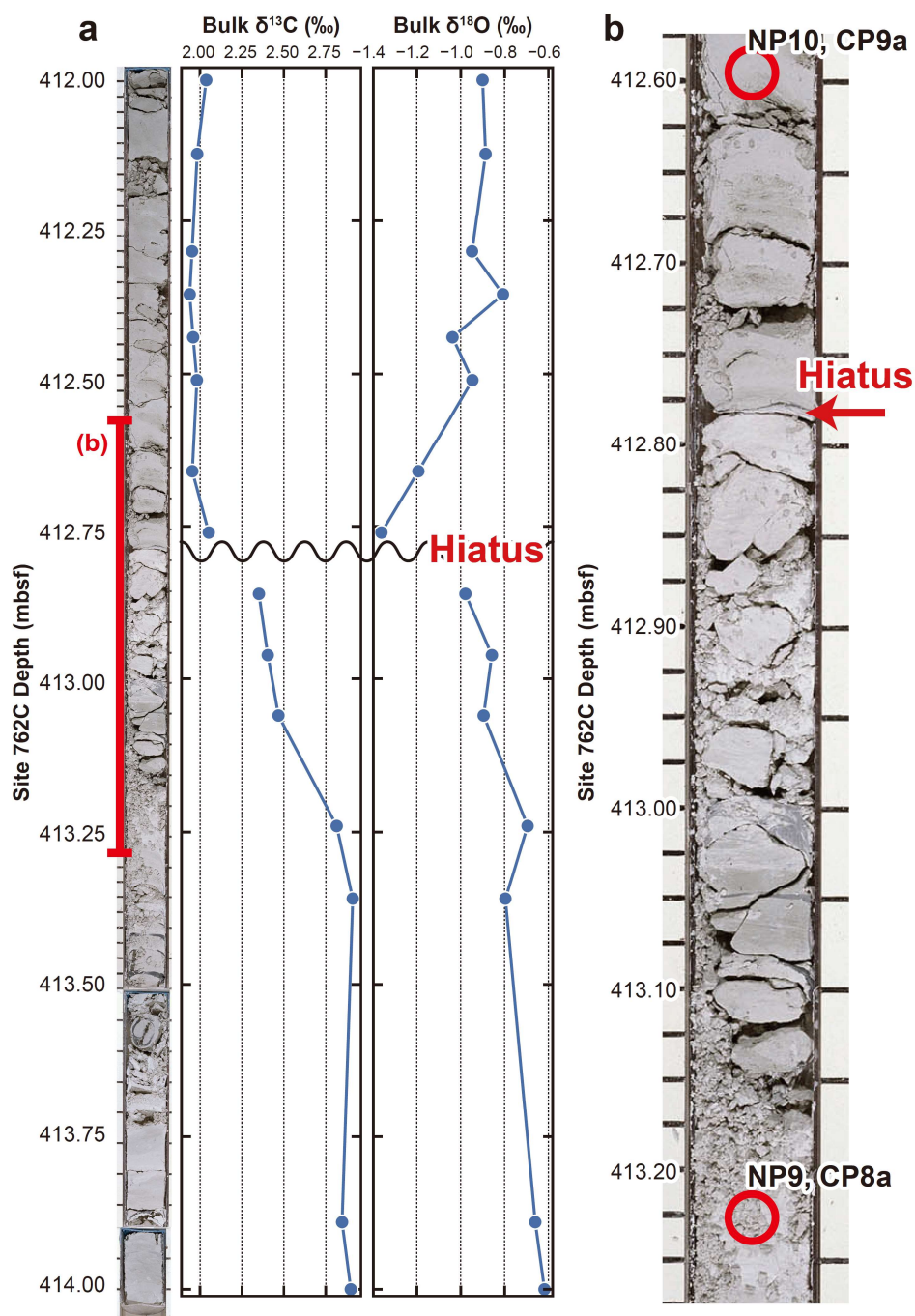


Figure S7. Core photograph and depth profiles of bulk $\delta^{13}\text{C}$ and $\delta^{18}\text{O}$ of Hole 762C Core 28X. (a) Whole core, (b) enlarged core photograph with nannofossil assemblage (Shamrock et al., 2012). Red circles indicate sampled points for biostratigraphic study. Core photographs are provided by IODP.

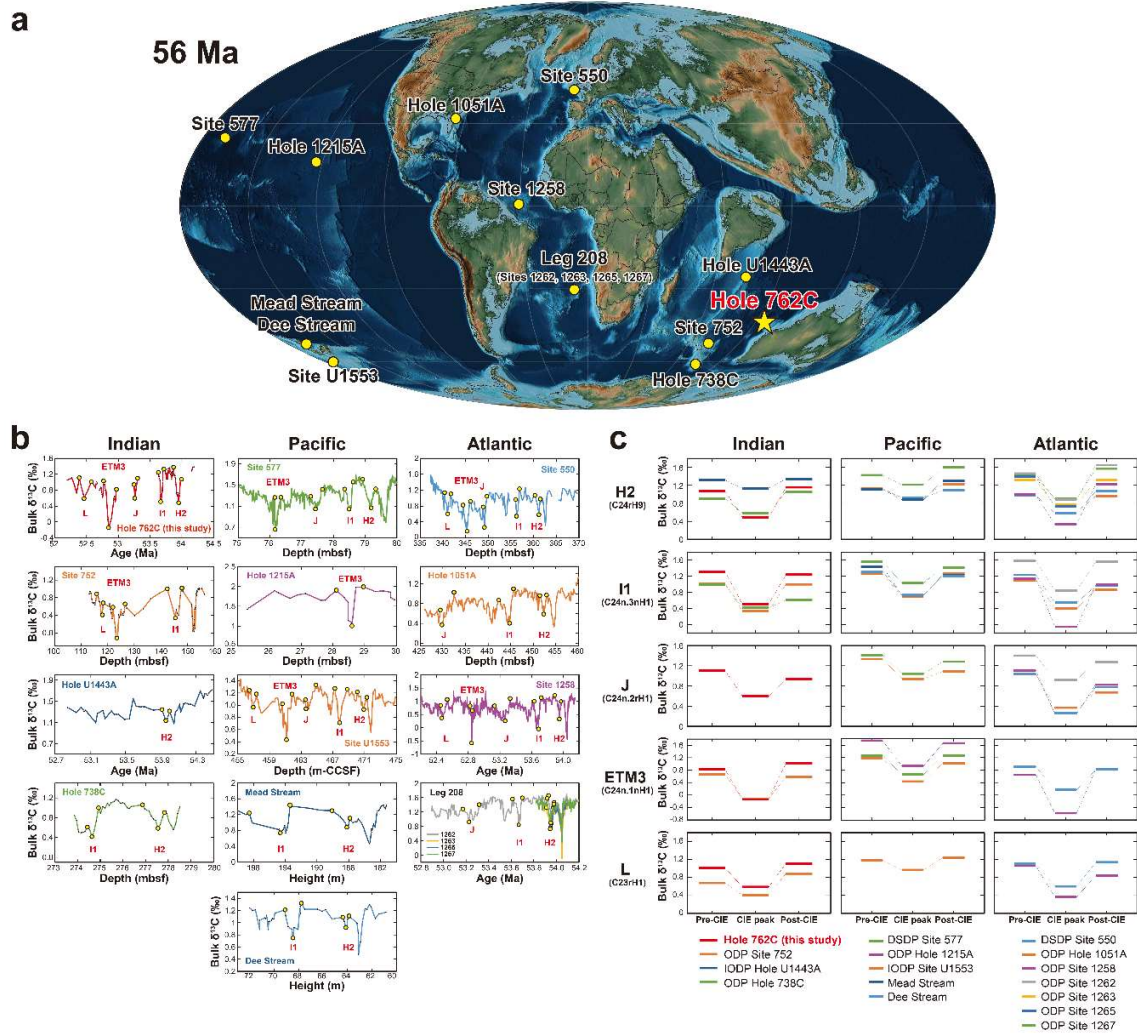


Figure S8. (a) Paleogeographic reconstruction at 56 Ma showing the locations where early Eocene hyperthermals have been documented in bulk carbonate $\delta^{13}\text{C}$. (b) Previously published bulk $\delta^{13}\text{C}$ profiles of hyperthermal horizons from the Indian, Pacific, and Atlantic Oceans. (c) Comparison of the magnitudes of carbon isotope excursions (CIE) for each hyperthermal event. Yellow dots in panel (a) indicate the data points used for the pre-CIE, CIE peak, and post-CIE values in panel (b). Paleogeographic data of panel (a) are based on Scotese (2001). Data sources: Site 752 and Hole 738C, Yasukawa et al., 2017; Hole U1443A, Barnett et al., 2020; Sites 577 and 550, and Hole 1051A, Cramer et al., 2003; Hole 1215A, Leon-Rodriguez & Dickens, 2010; Site U1553, Niederbockstruck et al., 2024; Mead Stream and Dee Stream, Nicolo et al., 2007; Sites 1258, 1262, 1263, 1265, and 1267, Westerhold et al., 2017.

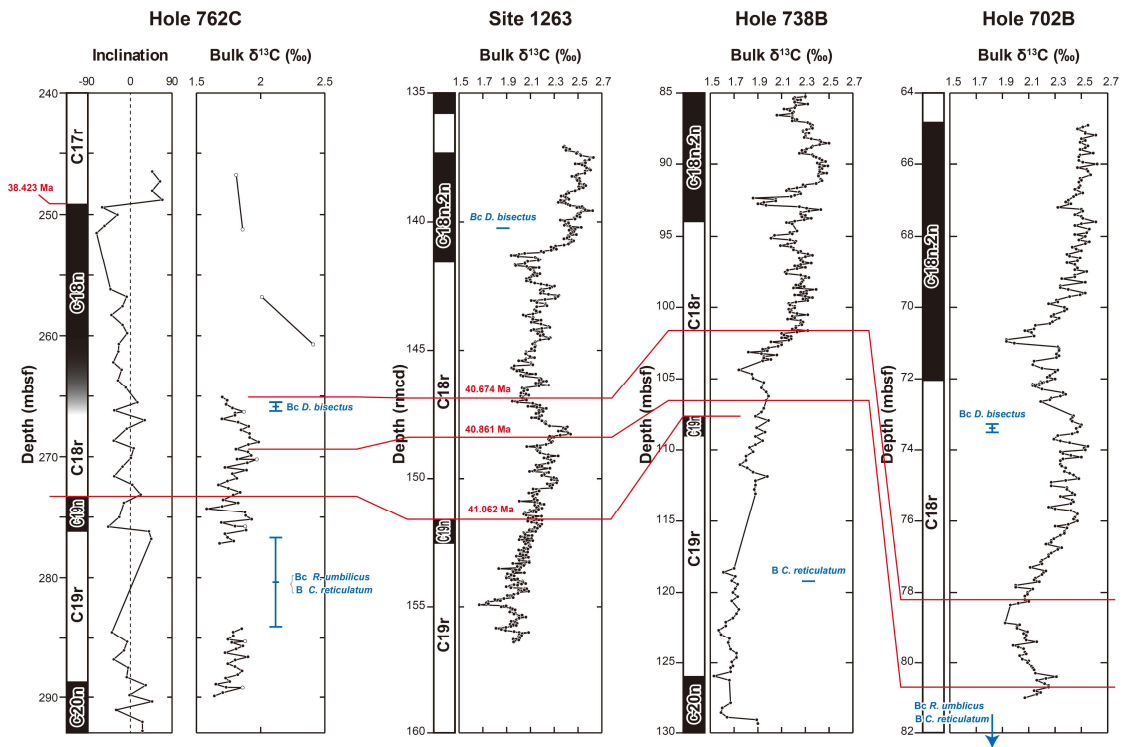


Figure S9. Correlation of middle Eocene interval of Hole 762C (this study) with Site 1263, Holes 702B, and 738B (Rivero-Cuesta et al., 2019 and references therein). Age tie points are indicated by red bars. Magnetic inclination and nannofossil events are also shown (Galbrun, 1992; Shamrock & Watkins, 2012). Plots of open circles in Hole 762C bulk $\delta^{13}\text{C}$ data are from Thomas et al. (1992).

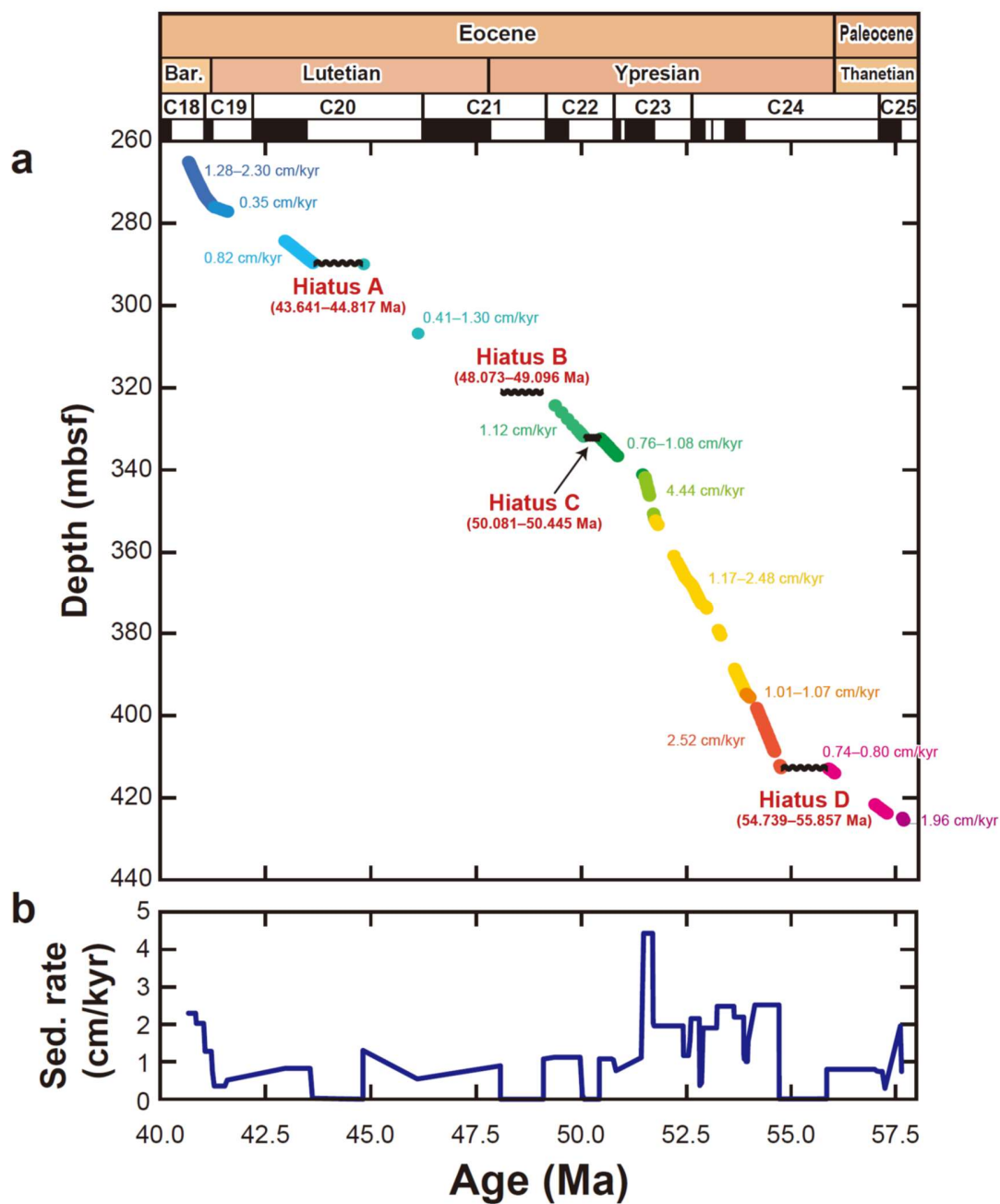


Figure S10. (a) Age–depth relationships and (b) estimated sedimentation rate of ODP Hole 762C.

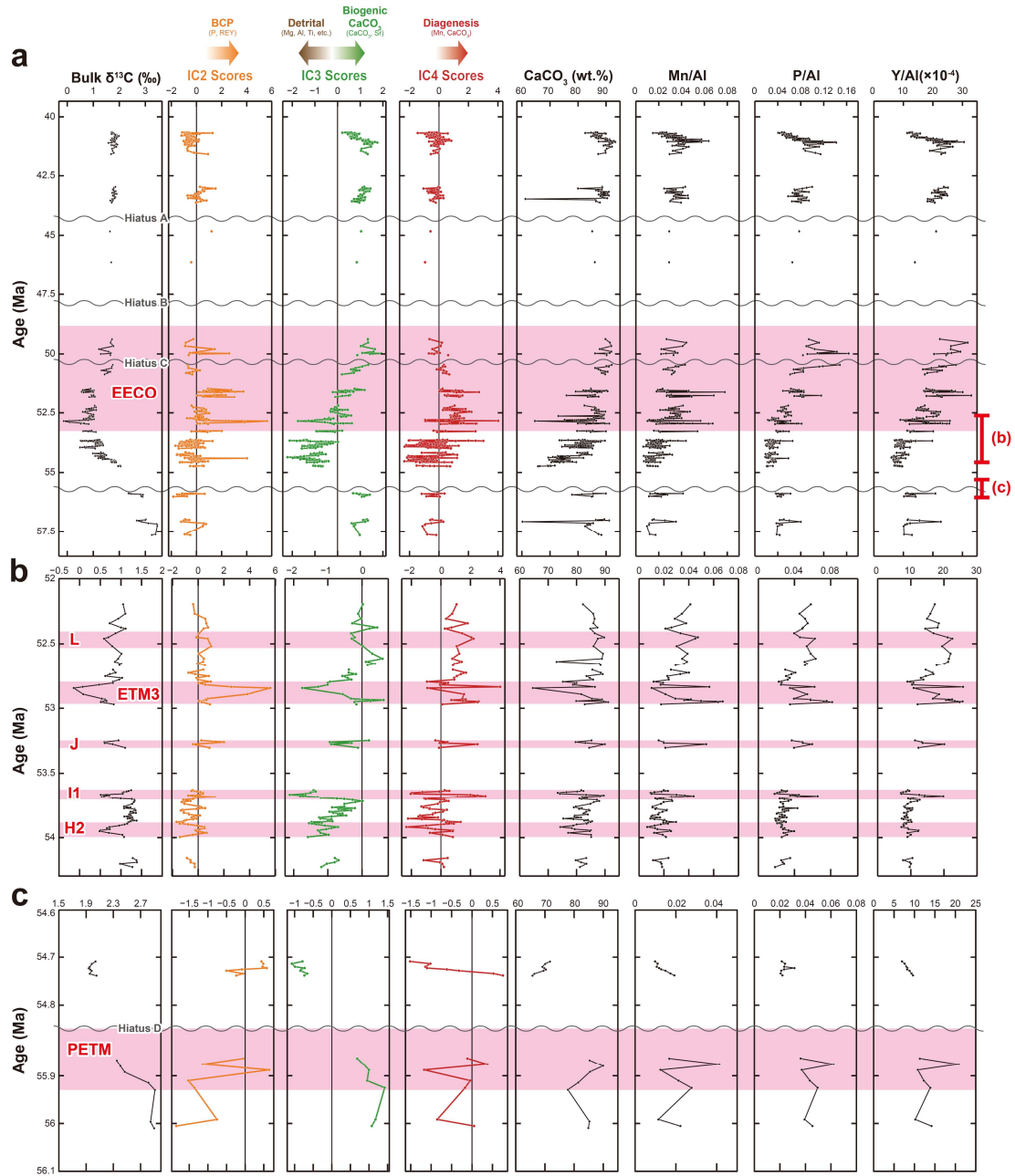


Figure S11. Bulk $\delta^{13}\text{C}$, IC2, IC3, IC4 scores, CaCO_3 abundances, and Al-normalized Mn, P, and Y concentration from the bulk chemical composition of ODP Hole 762C, plotted against estimated depositional age. (a) Whole studied sections. (b) Sections covering multiple hyperthermals (H2, I1, J, ETM3, and L). (c) The section covering PETM. Red bars in panel (a) indicate EECO, and in panels (b) and (c) indicate hyperthermals. Gray waved lines are hiatuses indicated by Shamrock et al. (2012).



Figure S12. Bulk $\delta^{13}\text{C}$, IC1, IC5, IC6 scores, and Al-normalized Co, Ni, Cu, Zn, Sr, Mo, Pb, and U concentration from the bulk chemical composition of ODP Hole 762C, plotted against estimated depositional age. (a) Whole studied sections. (b) Sections covering multiple hyperthermals (H2, I1, J, ETM3, and L). (c) Section covering the PETM. Gray lines in each panel are bulk $\delta^{13}\text{C}$ records. Red bars in the panel (a) indicate EECO, and in panels (b) and (c) indicate hyperthermals. Gray wavy lines are hiatuses indicated by Shamrock et al. (2012).

Table S1. Analytical results for JB-2, JB-3, and JMS-2 by ICP-QMS analyses. (uploaded separately)

Table S2. Principal component analysis (PCA) results for the bulk sediment composition at Hole 762C. (uploaded separately)

Table S3. Bulk $\delta^{13}\text{C}$ and $\delta^{18}\text{O}$ data of ODP Hole 762C. (uploaded separately)

Table S4. Major and trace element data of ODP Hole 762C. (uploaded separately)

Table S5. Chronostratigraphic events at Hole 762C Core 12X–29X. (uploaded separately)

References in Supporting Information

- Alibo, D. S., & Nozaki, Y. (1999), Rare earth elements in seawater: Particle association, shale-normalization, and Ce oxidation. *Geochimica et Cosmochimica Acta*, 63, (3–4). [https://doi.org/10.1016/S0016-7037\(98\)00279-8](https://doi.org/10.1016/S0016-7037(98)00279-8)
- Rudnick, R. L., & Gao, S. (2014), Composition of the Continental Crust. In *Treatise on Geochemistry: Second Edition* (Vol. 4, pp. 1–51). Elsevier Inc. <https://doi.org/10.1016/B978-0-08-095975-7.00301-6>
- Swanner, E. D., Webb, S. M., & Kappler, A. (2019), Fate of cobalt and nickel in mackinawite during diagenetic pyrite formation. *American Mineralogist*, 104(7), 917–928. <https://doi.org/10.2138/am-2019-6834>